North Brazil Current rings and transport of southern waters in a high resolution numerical simulation of the North Atlantic

Zulema D. Garraffo[a*], William E. Johns[a], Eric P. Chassignet[a],and Gustavo J. Goni[b]

[a]Rosenstiel School of Marine and Atmospheric Science, University of Miami, 4600 Rickenbacker Cswy., Miami, FL 33149, USA

[b] NOAA/Atlantic Oceanographic and Meteorological Laboratory, Miami, Florida 33149, USA

Output from a very high resolution (1/12 deg.) North Atlantic simulation with the Miami Isopycnic Coordinate Ocean Model (MICOM) is analyzed in a region of the Tropical Atlantic characterized by the presence of the North Brazil Current (NBC) retroflection and North Brazil Current rings. The model mean and seasonal circulations present a good qualitative agreement with observations. Quantitatively, the modeled NBC in summer and fall does not completely retroflect into the North Equatorial Counter Current, and the model upper 100 m NBC is more intense than the observed values by 3-4 Sv. The modeled NBC generates a variety of rings, which we classify as 'shallow', 'intermediate', 'deep', and 'subsurface'. An average of 8.3 rings of all types are generated per year, of which 6 are surface intensified, in good agreement with altimetry (5.7 rings per year, Goni and Johns, 2001). The transport of southern origin water by the the rings was estimated using two methods. First, the transport was computed kinematically from the rings' volume, resulting in an average transport of 6.6 Sv. Second, an estimation of southern water transport based on an explicit calculation of water mass content was done, resulting in an average transport of 7.5 Sv. The rings' contribution represents $\sim$40% of the total meridional transport from the surface to the intermediate water layers. Possible mechanisms operating in the model ring generation are briefly discussed.

1. INTRODUCTION

The circulation in the western equatorial and tropical Atlantic is very complex, in terms of its mean, seasonal cycle, and mesoscale variability (Schott *et al.*, 1998; Johns *et al.*, 1998). The dominant circulation feature near the western boundary is the North Brazil Current (NBC), which has sources in the equatorial region

*Corresponding author. Tel.: +1-305-361-4882. Fax: +1-305-361-4696. *Email address*: zgarraffo@rsmas.miami.edu.

and southern hemisphere. West of 35°W, and off the northern continental shelf of eastern Brazil, the surface NBC is principally composed of waters from the equatorial Atlantic, via the South Equatorial Current. The subsurface NBC receives waters from the southern hemisphere North Brazil Undercurrent (NBUC) and, to a lesser extent, the South Equatorial Current. Below the thermocline, sources for the NBC are the southern hemisphere NBUC and probably the Equatorial Intermediate Current (Schott *et al.*, 1998).

In the upper layers, the North Brazil current seasonally retroflects into the North Equatorial Counter Current (NECC) (Richardson and Walsh, 1986; Garzoli and Katz, 1993; Johns *et al.*, 1998). Large anticyclonic eddies, the NBC rings, detach from the retroflection and travel northwestward, carrying waters of southern hemisphere origin (Johns *et al.*, 1990; Didden and Schott, 1993; Richardson *et al.*, 1994; Fratantoni *et al.*, 1995; Goni and Johns, 2001). Surface Amazon river waters are partly entrained into the rings' periphery (Steve and Brooks, 1972; Borstad, 1982; Kelly *et al.*, 2000; Fratantoni and Glickson, 2002). The subsurface NBC contributes to the Equatorial Undercurrent (EUC) and to the North Equatorial Undercurrent (NEUC), as discussed by Cochrane *et al.* (1979), Schott *et al.* (1998), Johns *et al.* (1998), and Bourles *et al.* (1999 a).

NBC rings are believed to be one of three principal mechanisms for transporting upper ocean equatorial and South Atlantic waters into the North Atlantic as part of the Meridional Overturning Cell (MOC). Other mechanisms include coastal currents along the South American shelf (Csanady, 1985; Candela *et al.*, 1992) and offshore retroflection into the NECC followed by northward Ekman transport in the ocean interior (Mayer and Weisberg, 1993). It is therefore important to quantify the NBC rings' contribution to the MOC.

The Atlantic MOC involves the cross equatorial northward flow of approximately 14 Sv of upper ocean waters (Schmitz, 1996), composed of intermediate waters entering through the Drake Passage and thermocline waters entering off the southern tip of Africa (Rintoul, 1991; Gordon 1986; Gordon *et al.*, 1992). This upper branch of the MOC together with the deep northward flow of Antarctic Bottom Water balance the southward flow of approximately 18 Sv of North Atlantic Deep Water (Schmitz, 1996).

Several estimates of the northward NBC ring transport have been made from observations. Johns *et al.* (1990) estimated that for each ring generated in a year, there is a contribution to the upper branch mass transport of about 1 Sv (1 Sv= $1^6 m^3/s$). Didden and Schott (1993) pointed out that water mass studies are required for a quantitative estimation of water mass anomalies. They identified 5 rings in a 2.5 year period using GEOSAT altimeter data, and estimated the transport by rings to be on the order of 3 Sv. Fratantoni *et al.* (1995) identified rings of different penetration depths using data from a mooring located in the NBC retroflection region. They found a correspondence between the deeper rings and those identified from GEOSAT altimetry by Didden and Schott (1993), and estimated the transport by rings to be between 3 and 4 Sv. Richardson and Schmitz (1993) and Richardson *et al.* (1994) showed anticyclonic eddy signatures reaching 800-900 m depth, and suggested a ring-induced northward transport of

approximately 3 Sv. Recent satellite measurements (TOPEX/ Poseidon and SeaWIFS) suggest that the number of formed rings is closer to 5-6 per year with an associated 5-6 Sv of northward transport (Goni and Johns, 2001; Fratantoni and Glickson, 2002). According to all of these estimates, the NBC rings can therefore contribute to as much as one-third of the net 14 Sv of the warm limb of the Atlantic overturning cell.

Until recently, there has not been sufficient hydrographic data available to permit study of the water mass composition of NBC rings and to provide a quantitative estimate of the water mass anomaly. Such data were finally acquired in the 1998-2000 North Brazil Current Rings Experiment, which was designed to provide an extensive observational data set to examine the ring structures. According to Johns *et al.* (2003, this volume), the hydrographic measurements suggest that the NBC ring-induced northward transport can reach 9 Sv, a much larger value than that previously assumed. Despite these recent measurements, many uncertainties remain. For example, the ring vertical structure was found to be very complex (Wilson *et al.*, 2002), implying the need to survey rings of various types. In addition, the magnitude and variability of the MOC over the Atlantic is not precisely known. Numerical ocean models can provide a source of knowledge complementary to observations, allowing complete diagnostics for the study of several aspects of the circulation.

Numerical ocean simulations have been successful in producing North Brazil Current rings. Fratantoni *et al.* (1995) found that NBC rings were generated by the U.S. Navy's layered ocean model (.25 deg. resolution) at a rate of 2-3 rings per year. Barnier *et al.* (2001) present results from three eddy-permitting models over the same Atlantic domain which differ in the vertical coordinate formulation, all with 1/3 deg. resolution at the equator. These models show significantly different NBC ring activity, ranging from almost no ring activity to a generation rate of 6.4 rings per year, the difference being mainly attributable to different horizontal diffusion formulations. The authors find that the eddy fields vary among the models, but the mean transport of the North Brazil Current remains proportional to the model values of the MOC. The NBC rings are also important for their effect on the variability in the Caribbean, which they influence either by entering the region or by affecting the transports through the Lesser Antilles passages. Rings in the Caribbean Sea and their relation to the NBC rings were recently studied by Carton and Chao (1999) and Murphy *et al.* (1999).

Although these model studies provide information on generation mechanisms, generation rate, and seasonality of NBC rings, they have not carefully examined the water mass structure of the rings and their role in the MOC. In this paper, we take advantage of a fine mesh (1/12 deg.) North Atlantic numerical simulation performed with the Miami Isopycnic Coordinate Ocean Model (MICOM) to study several aspects of the North Brazil rings, such as formation rates, structures, trajectories, and effect on the Lesser Antilles passage transports, with emphasis on a quantitative estimation of the rings' water mass transport and contribution to the meridional transport.

In order to address the issues noted above, the model results are first validated

by comparing the simulated circulation with *in-situ* measurements and with altimeter data. Having gained confidence that the model mean and seasonal circulations are realistic, we estimate the volume and water mass transport of thermocline waters of southern hemisphere and equatorial origin by rings. The results from the water mass analysis are used to obtain the model ring transport during 6 model years and relate this transport to the meridional transport, allowing us to conclude that an average of 7.5 Sv ($\sim$40%) of the model North Atlantic upper and intermediate water meridional transport is southern water transported by the model NBC rings.

The paper is organized as follows. The main aspects of the numerical simulation are introduced in section 2. In section 3 and 4, the modeled tropical circulation and NBC rings are compared to published hydrographic observations and to altimetry measurements. In these two sections, we also discuss the mean and seasonal circulation in the surface and subsurface layers, analyze the sea surface height (SSH) fields and variability, and study the vertical structure and trajectories of the modeled NBC rings and their effect on the transports through the Eastern Antilles passages. In section 5, a water mass analysis of the rings is performed, including transport estimates by water mass analysis and by volumetric considerations. We conclude with a discussion relating the results to the upper and intermediate meridional transport.

2. MODEL CONFIGURATION

The Miami Isopycnic Coordinate Ocean Model (MICOM) is well documented in the literature. For a review, the reader is referred to Bleck *et al.* (1992) and Bleck and Chassignet (1994). The fundamental reason for modeling ocean flow in density coordinates is that this system suppresses the diapycnal component of numerically caused dispersion of material and thermodynamic properties, such as temperature and salinity. This characteristic allows isopycnic models to prevent the warming of deep water masses, as has been shown to occur in models framed in Cartesian coordinates (Chassignet *et al.*, 1996). Furthermore, the association of vertical shear with isopycnal packing and tilting in the ocean makes isopycnic models appropriate for studies of strong baroclinic currents such as the Gulf Stream.

The computational domain is the north and equatorial Atlantic Ocean basin from 28°S to 65°N, including the Caribbean Sea and the Gulf of Mexico. The horizontal grid (6 km on average) is defined on a Mercator projection with resolution given by $1/12^{\circ} \times 1/12^{\circ} cos(\phi)$, where ϕ is the latitude. The bottom topography is derived from a digital terrain data set with 5' latitude-longitude resolution (ETOPO5). The vertical density structure is represented by 15 isopycnic layers, topped by an active bulk Kraus-Turner type surface mixed layer, vertically homogeneous, but of density varying in the horizontal, that exchanges mass and properties with the isopycnic layers underneath (Kraus and Turner, 1967; Bleck *et al.*, 1992). The isopycnic layers have potential density values of 24.70, 25.28, 25.77, 26.18, 26.52, 26.80, 27.03, 27.22, 27.38, 27.52, 27.64, 27.74, 27.82, 27.88, and 27.92.

The vertical discretization was chosen to provide maximum resolution in the

upper part of the ocean. Open ocean boundaries are treated as closed, but are outfitted with 3° buffer zones in which temperature (T) and salinity (S) are linearly relaxed toward their seasonally varying climatological values (Levitus, 1982), with damping/relaxation time from 5 days at the wall to 30 days at the inner edge of the buffer zone. The buffer zones restore the T and S fields to climatology in order to approximately recover the vertical shear of the currents through geostrophic adjustment. The surface boundary conditions are based on the COADS monthly climatological data sets (da Silva *et al.*, 1994). The model was spun up from rest for a total of 21 years and our analysis focuses on the final 6 years.

The high horizontal grid resolution drastically improved the model's behavior in comparison to that of previous coarse-resolution simulations. The major improvements are: (a) a correct Gulf Stream separation (Chassignet and Garraffo, 2001), and (b) higher eddy activity. These results support the view that an inertial boundary layer, which results from the fine resolution, is an important factor in the separation process (Özgökmen *et al.*, 1997), and that resolution of the first Rossby radius of deformation is necessary for a correct representation of baroclinic instabilities. The 6-year mean transport of 27.4 Sv through the Florida Straits is close to the observed value of 30 Sv, with a seasonal cycle of the same magnitude and phase as those seen in cable data (Larsen, 1992). The behavior of numerical Lagrangian drifters and a comparison to that of real drifters is presented in Garraffo *et al.*, (2001a,b), and the probability density functions for the simulated Lagrangian data are discussed in Bracco *et al.* (2003).

3. THE NORTH BRAZIL CURRENT SYSTEM FROM THE MODEL AND OBSERVATIONS: THE SEASONAL CIRCULATION

In this section, the modeled surface and subsurface circulations in the NBC region are compared to published observations. These comparisons are important in order to assess the validity of the model results and, therefore, of the model output analysis. The simulation has already been shown to produce good agreement between the surface fields and drifter observations for the North Brazil current region (Garraffo *et al.*, 2001a): the simulated and observed mean velocities were found to agree, and the model eddy kinetic energy was found comparable to but slightly higher than that observed. The Lagrangian velocity time scales computed from the velocity autocovariances were found to be about 1-2 days for *in-situ* drifters, and 2-3 days for the numerical drifters for the NBC region. The time scales are shorter in the western boundary currents than in the ocean interior, especially in the modeled NBC region. The short time scale is interpreted as being due to the fast decorrelation between particles trapped in NBC rings and particles outside the rings.

The circulation in the NBC region as inferred from the model is compared to recent observations as described in Johns *et al.* (1998), Schott *et al.* (1998), and Bourles *et al.* (1999 b). Following Johns *et al.* (1998, Figure 18), the model surface and subsurface ($\sigma_0 = 26.18$, layer 5, about 200 m depth) velocities seasonally averaged over the 6-year period are shown in Figure 1. As in the observations,

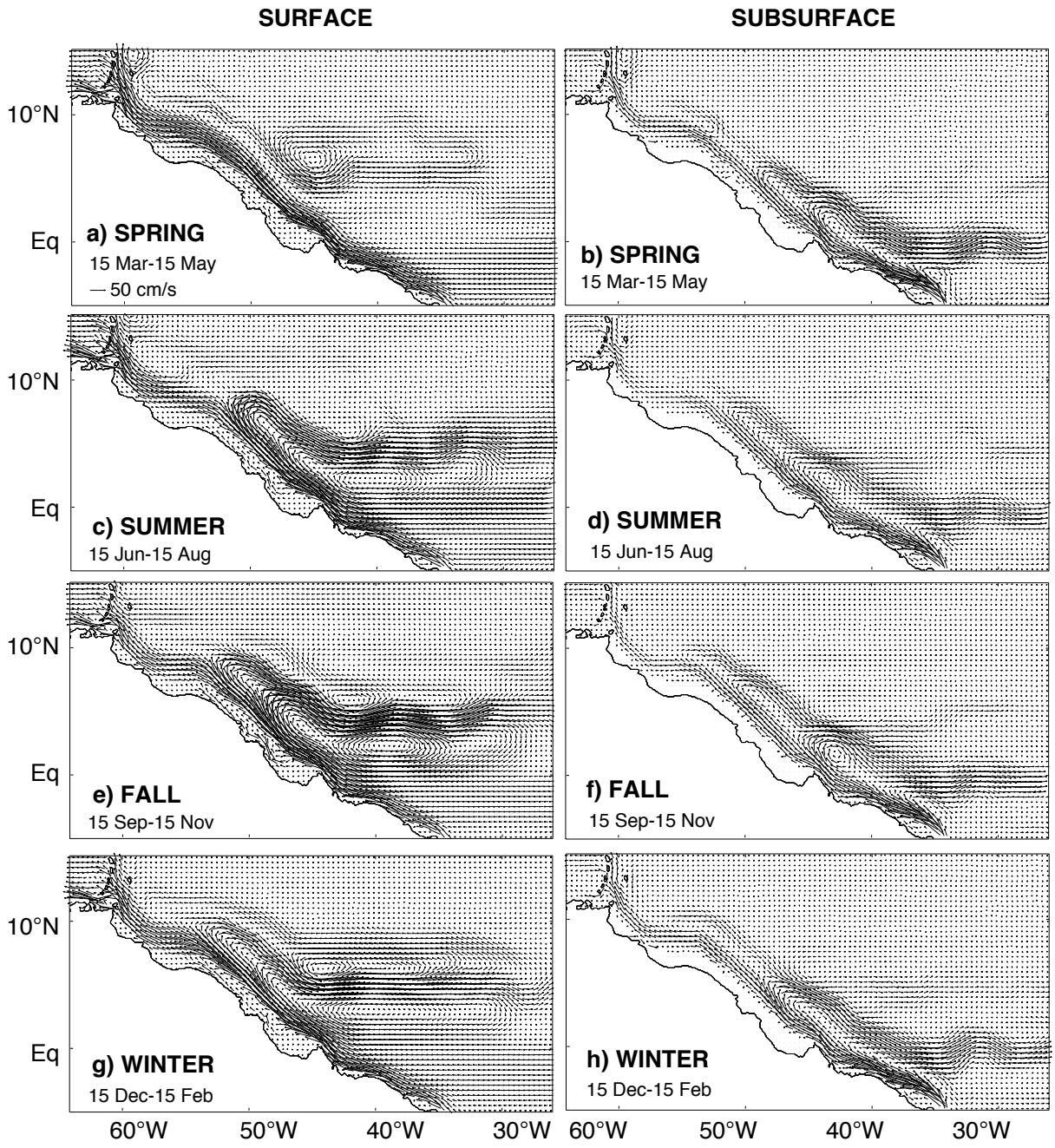

Figure 1. a),c),e),g): Model surface velocity averaged for 2-month periods during 6 model years; b),d),f),h): same for subsurface velocity ($\sigma_0 = 26.18$, layer 5).

the modeled surface retroflection develops in (boreal) summer and fall and remain present in winter, but is absent during spring. This is further illlustrated in Figure 2 a,b, showing one realization of the model instantaneous surface circulation for spring (no clear retroflection at $\sim 5^\circ$N) and one for fall (retroflection at $\sim 5^\circ$N). However, the seasonal circulation, being a time average, includes the signature of

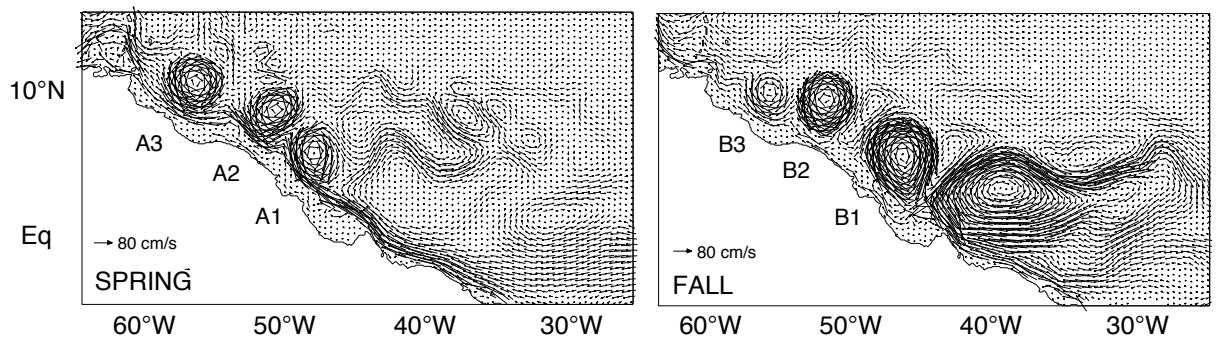

Figure 2. Instantaneous model surface velocity on one day in spring (left, year 16, May 10), and one day in fall (right, year 16, Nov 15).

the NBC rings as they propagate northwestward. For example, the band of southeastward flow found offshore of the NBC between 5-10°N during spring (Figure 1a) is a rectified signature of NBC rings (Figure 2a), even though the retroflection is absent at this time. The western tip of the NBC surface retroflection derived from the model results is located at approximately 50°W in summer, and moves westward in fall and winter, reaching 53°W in winter before disappearing in the spring (Figure 1 c,e,g,a respectively).

The modeled subsurface circulation is in good qualitative agreement with observations, as evidenced by: a) a permanent retroflection of the westward subsurface NBC just north of the equator into the eastward Equatorial Undercurrent (EUC) (Schott *et al.*, 1998; also Cochrane *et al.*, 1979, Molinari and Johns, 1994) , and b) a seasonally varying retroflection into the North Equatorial Undercurrent (NEUC), in which the subsurface NBC penetrates farther to the west in summer and fall than in spring [in agreement with Johns *et al.* (1998)].

The model NBC upper 100 m transports are compared to the observed values in Table 1. Since the modeled mixed layer depth in the region is on average approximately 80 m, the upper 100 m circulation is very similar to that in the mixed layer. In spring, when the surface retroflection is absent, the modeled upper 100 m transport is 13 Sv at 44°W and 11 Sv at 52°W (Table 1, corresponding to Figure 1a), including the coastal current, which is weak in the model (about 0.6 Sv in all seasons). This transport is slightly higher (by about 3 Sv) than the values of 10 Sv and 8 Sv given in Johns *et al.* (1998) for similar longitudes (44°W and 48°W). Recently published observations at 44°W by Bourles *et al.* (1999 b) give a similar value, an average of 10.6 Sv from two sections in January, while Bourles *et al.* (1999 a) give 6 Sv at 45°W for one section in April. During the summer (June-August) and fall (Sept-Nov), when the surface retroflection develops, the modeled NBC upper 100 m transport is 18 Sv at 44°W. The value given by Johns *et al.* (1998) is 14 Sv at 44°W (Table 1), which is consistent with the 13.7 average of 4 sections at 44°W and 45°W in August and September given in Bourles *et al.* (1999 a, b). The modeled circulation for the incoming NBC is therefore $\sim$ 3-4 Sv more intense than that derived

Table 1
Transport (Sv) from model and observations

	spring		fall	
	model	obs	model	obs
NBC, 44°W	13	6^a-10^b	18	14
NBC, 48 to 52°W	11	8	8	0
NECC,44°W			15	19

Model and observed (from Johns *et al.*, 1998, Schott *et al.*, 1998, Bourles *et al.*, 1999 a,b) upper 100 m transports in Sv, for the NBC at two longitudes and for the NECC, in spring and fall.
[a]: Bourles *et al.*, 1999 a, [b]: Schott *et al.*, 1998.

from *in-situ* observations in both seasons. The modeled total upper and intermediate water meridional transport across the Atlantic, discussed in section 6, is also 3-5 Sv more intense than observational estimates. During the summer and fall, the modeled surface NBC, after retroflecting, contributes to the NECC, into which a small branch of the NEC merges (Figure 1c, 1e, 52°W 10°N). At 44°W (and $\sim$ 5°N), the modeled NECC upper 100 m eastward transport during summer and fall is 15 Sv, while an observational value of 19 Sv is obtained by averaging 4 sections in August and September from Bourles *et al.* (1999 a,b), and 1 section in October by Schott *et al.* (1998). The eastward transport of the NECC is therefore about 4 Sv weaker than the observed value, due in part to an incomplete retroflection of the NBC in the model. At 52°W, the model shows 8 Sv continuing westward in the NBC in the fall while observations suggest that essentially all of the NBC waters retroflect, leaving no net transport along the western boundary. Therefore, the modeled NBC contributes about 10 Sv to the NECC during fall. The contribution from the modeled NEC from the north, plus other possible recirculations, is 5 Sv (as obtained by balancing the mass transports), in agreement with the 5 Sv suggested by observations (also by transport balance).

In summary, there is a good qualitative agreement between the model and the observed seasonal circulation, with the exceptions that the NBC surface layer in summer and fall does not completely retroflect into the NECC as indicated by observations, and that the modeled upper 100 m NBC transport slightly exceeds the observed seasonal values by 3 to 4 Sv. The incomplete retroflection of the modeled NBC in summer and fall appears to be linked to the weaker transport of the NECC in the model (15 Sv) than in observations (19 Sv). The weaker value in the model implies that less water from the NBC is required to separate from the coast and flow eastward into the interior. The comparison of the NECC transport to observations is complicated by the zonal variation of the NECC transport in the model, which increases eastward from 15 Sv at 44°W to 19 Sv at 40°W due to local recirculations. Still, at 44°W the model NECC transport is about 4 Sv weaker than the observed value. This discrepancy can in part be due to the COADS wind forcing, since Townsend *et al.* (2000) find that the North Atlantic Tropical gyre closed

by the NECC shows an annual mean Sverdrup transport of 6 Sv for COADS, the lowest value of the 6 Sv - 17 Sv range given by 11 wind climatologies.

4. THE NORTH BRAZIL RINGS, SEA SURFACE HEIGHT VARIABILITY, AND EFFECT ON TRANSPORTS THROUGH THE LESSER ANTILLES PASSAGES

The western boundary circulation west of 50°W breaks into North Brazil rings, large anticyclonic eddies that are generated in the retroflection region and travel northwestward. NBC rings have been studied from current meter data (Johns *et al.*, 1990; Fratantoni *et al.*, 1995), from floats (Richardson *et al.*,1994), from altimetry (Didden and Schott, 1993; Goni and Johns, 2001), and from ocean color imagery (Fratantoni and Glickson, 2002). NBC rings are important because they transport water masses northward from the region of generation, contributing to the interhemispheric exchange, and because of environmental issues associated with the impact of the rings on the Lesser Antilles.

As can be seen in the model instantaneous circulation realizations (Figure 2 a,b) for one day in spring and one in fall, the NBC rings are generated off South America/Brazil near 50°W and travel northwestward. The figures show NBC rings shortly after generation (rings A1, B1), and others (A2, A3, B2, B3) that were generated earlier and have progressed northwestward. The anticyclonic NBC rings have an associated positive SSH anomaly. In this section, we compare results from the model SSH with altimeter data, examine the vertical structure of the modeled rings and their trajectories, and discuss the effect of the rings on the transport through the Lesser Antilles passages.

4.1. Sea surface height space-time diagrams

A detailed identification of NBC rings in the model was done from animations of daily maps of SSH and vertical sections of velocity, with results that will be discussed in detail in sections 4.3 and 5. A total of 45 rings were identified from SSH during the 6 analyzed years, corresponding to 7.5 rings per year with a surface signal. For some of the rings the SSH signal is very weak. During that 6 year period, a total of 5 additional rings with no surface signal were identified. Comparable results were obtained from altimetry by Goni and Johns (2001), who identified a total of 34 NBC rings during the 6 years between 1993 and 1999, or 5.7 rings per year.

The information on NBC ring generation and propagation can be compactly displayed by SSH space-time diagrams. The model time series of SSH for sections extending from the NBC retroflection region to the Eastern Antilles (Figure 3a) are shown in Figure 3 b. North Brazil rings are characterized by positive SSH differences with respect to the surrounding values, superimposed on the annual cycle, as the rings travel from the eastern to the western sections essentially parallel to the coast (Figure 3b, 10 lower panels, sections 5-14). The anomalies in sections 10-14 correspond either to rings already separated from the NBC retroflection or to the retroflection itself. As the rings approach the Lesser Antilles, they tend to turn and propagate northward along the island arc (3rd and 4th panel from top,

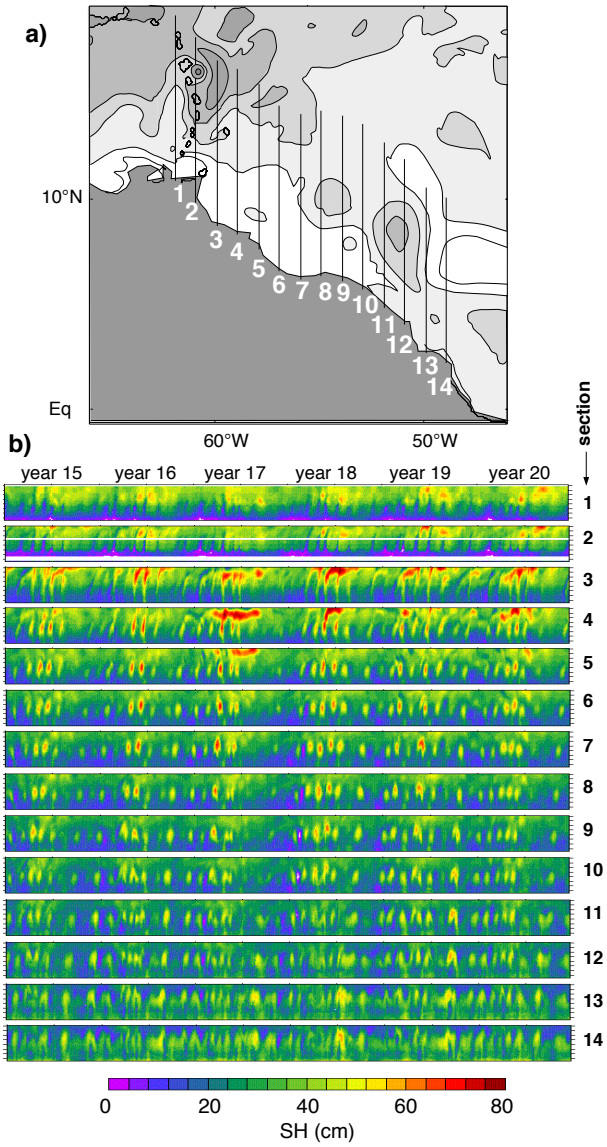

Figure 3. a) sections (extending $\sim 8^\circ$ in latitude), covering from 62°W (section 1) to 49°W (section 14); b) SSH time series for the 6 model years, over the sections, from the eastern section (at 49°W, section 14, lower panel) to the western section (at 62°W, section 1, top panel).

sections 3 and 4). These rings often interact and merge with each other in this area, and tend to stall and coalesce into a large positive sea level anomaly just east of the northern Lesser Antilles. Inside the Caribbean (top panel, section 1), generally smaller SSH anomalies are seen propagating westward. These smaller anomalies often originate as a splitting from a ring that remains for some time to the east of the Lesser Antilles, as seen by examining animations of the daily SSH maps. It is also apparent in Figure 3b that the time interval between suc-

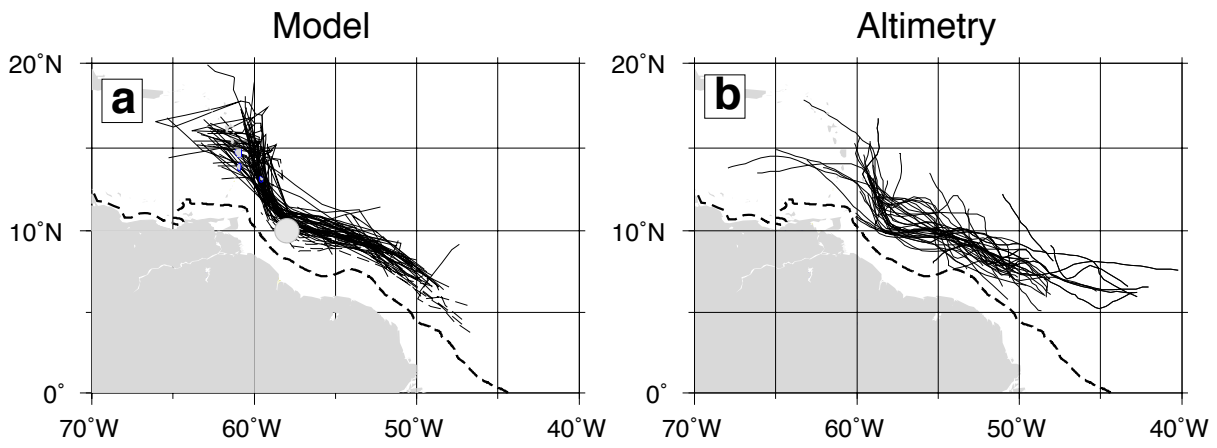

Figure 4. a) Ring trajectories obtained from modeled SSH (solid lines), and additional trajectories for rings with no SSH signal (dashed-dotted lines); the 500 m isobath is shown as a thick line. The circle (58°W, 10°N) is marked in relation to Figure 9. b) Ring trajectories derived from TOPEX/Poseidon (Goni and Johns, 2001).

cessive rings varies, with ring generation showing an apparent seasonal cycle and significant year-to-year variability. This interannual variability in the model with climatological forcing can be caused by: a)model internal dynamics; b)the model not having reached complete equilibrium.

The modeled ring trajectories derived from SSH horizontal maps and animations are shown in Figure 4 a, while trajectories derived from TOPEX/Poseidon data (adapted from Goni and Johns, 2001) are shown in Figure 4 b. The trajectories of modeled rings not presenting a SSH signal were added in dashed-dotted lines in Figure 4a and will be discussed in section 4.3. Similar to the signals of observed rings, the signals of the modeled rings follow the topography, but the dispersion of the modeled trajectories around a mean path is smaller than in the observations. Reasons for the difference could be the lack of high frequency and interannual forcing in the model, or error associated in determining the rings' center from TOPEX/Poseidon due to the sparse groundtracks.

Typical model SSH differences between the ring center and the surrounding waters vary between 15 and 30 cm. Altimetry measurements indicate that SSH anomalies at the center of the rings are smaller, of order 5 to 15 cm (Didden and Schott, 1993; Goni and Johns, 2001). Model and observed ring SSH signals are further discussed in the next section.

4.2. Surface height variability from the model and observations

A comparison between the modeled SSH variability (cm) and that obtained from TOPEX/Poseidon is shown in Figure 5. The North Brazil current system is characterized in the model and in the observations by a region of high variability extending from the NBC retroflection location ($\sim 8°$N, 50°W) to the Antilles. NBC rings identified in Figures 3 and 4, superimposed on the seasonal cycle, are the major

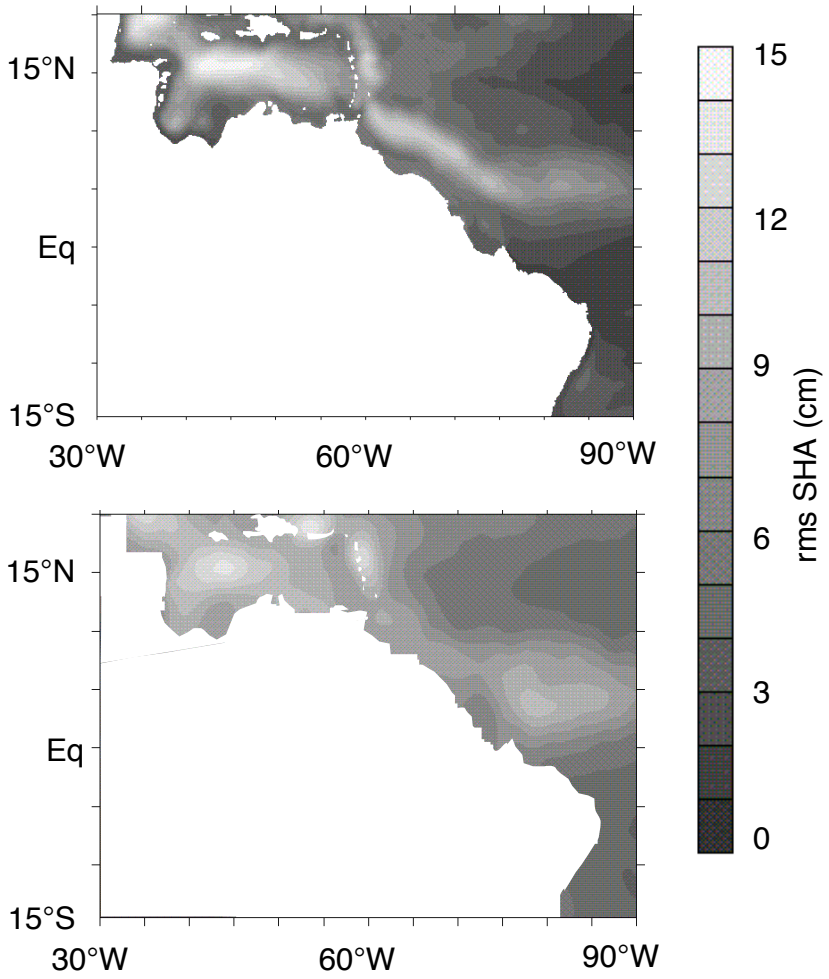

Figure 5. a) SSH variability (rms of sea height) for the North Brazil Current and Caribbean region (cm) obtained from the model; b) the same derived from the first five years of TOPEX/Poseidon sea hight anomaly data.

contributors to the SSH variability between 50°W and the Lesser Antilles. Also consistent with observations, high eddy activity is present in the Caribbean Sea and in a band extending North-East of the Antilles. A secondary maximum of variability is present east of the North Eastern Antilles (north of Barbados) both in the model results and in the observations. This secondary maximum is related to the stalling of rings reaching the eastern Antilles, similar to results found by Simmons and Leben (personal communication) from TOPEX/Poseidon altimetry, extending the Simmons and Nof (2002) study on the mechanisms for ring interaction with the Lesser Antilles. The region of high variability that extends off the coast from the retroflection location to the eastern Antilles is narrower and more intense in the model than in the altimeter observations. This difference can in part be attributed

to the model climatological forcing and the absence of high frequency and interannual variability. A model SSH ring signal larger than the altimetry signal can also contribute to this difference. High values of altimeter-derived SSH variability that were present near the mouth of the Amazon River have been filtered out because they are mainly due to tidal aliasing. (Arnault and Le Provost, 1997).

4.3. Ring types, associated sea height anomaly, and trajectories

The North Brazil rings that occur in the model show different vertical characteristics, which we classify into four different types: 'shallow', 'intermediate', 'deep', and 'subsurface'. The 'shallow', 'intermediate', and 'deep' rings are characterized by velocity signals larger than 10 cm/s extending from the surface to about 200, 500, and 900-1000 m respectively. The 'subsurface' rings show a very small (or even non-existent) surface velocity signal and a maximum velocity at around 200 m ($\sigma_0 = 26.52$) for most rings (but varying between about 100 m ($\sigma_0 = 25.28$) and 300 m ($\sigma_0 = 26.80$)), and signals larger than 10 cm/s extending to about 800 m ($\sigma_0 = 27.22$). Rings of all types are present among the 45 modeled rings identified from SSH during the 6 model years. Another 5 rings with no surface signal were identified from subsurface salinity and velocity fields during the 6 model years, by examining horizontal maps and movies. Therefore, the total number of modeled rings of all types is 50 during the 6 model years, or an average of 8.3 rings per year. Figure 6 shows, for each ring type, a characteristic vertical cross-section at 10°N in which the velocity structure and layer interfaces are displayed together with the corresponding SSH signal. The trajectories for all the rings of each type are also displayed to the right in Figure 6. Trajectories are marked with dashed lines after a ring splits or merges with another ring or feature. Of the 5 subsurface rings not identified from SSH, 3 rings presented no surface signal. For the other 2 rings the subsurface signal and the SSH anomaly, initially co-located, traveled on different paths, the subsurface ring nearer to the South American coast and slightly slower than the surface signal. These features later merged with the next ring generated from the NBC retroflection. The subsurface trajectories for the 5 subsurface rings with no clear SSH signal are marked with a dashed-dotted line in Figure 6. These 5 rings are generated at a location to the east of the other rings.

The model ring types and structures are in close correspondence with those that have been observed using shipboard hydrographic and direct velocity measurements by Wilson *et al.* (2002). Wilson *et al.* (2002) found a subsurface ring in Dec. 1998 that had a velocity core at 150 m depth and 40 cm/s velocities extending to 500 m; they also found rings of 'deep' type (40 cm/s velocities down to 1600 m) and 'shallow' type (significant velocities confined above 200 m). The altimeter-derived SSH anomaly difference between ring center and the surrounding waters, associated with the four rings reported by Wilson *et al.* (2002), range from 2 cm for the 'subsurface' ring to 12 cm for the other types (Johns *et al.*, 2003). In the model, the SSH center-to-periphery differences associated with the rings are typically 15 cm for those subsurface rings that present a surface signal, and 20 to 30 cm for the ring types that have maximum velocities at the surface (the 'shallow', 'intermediate', and 'deep' rings). The corresponding SSH anomaly differences at 10°N obtained by

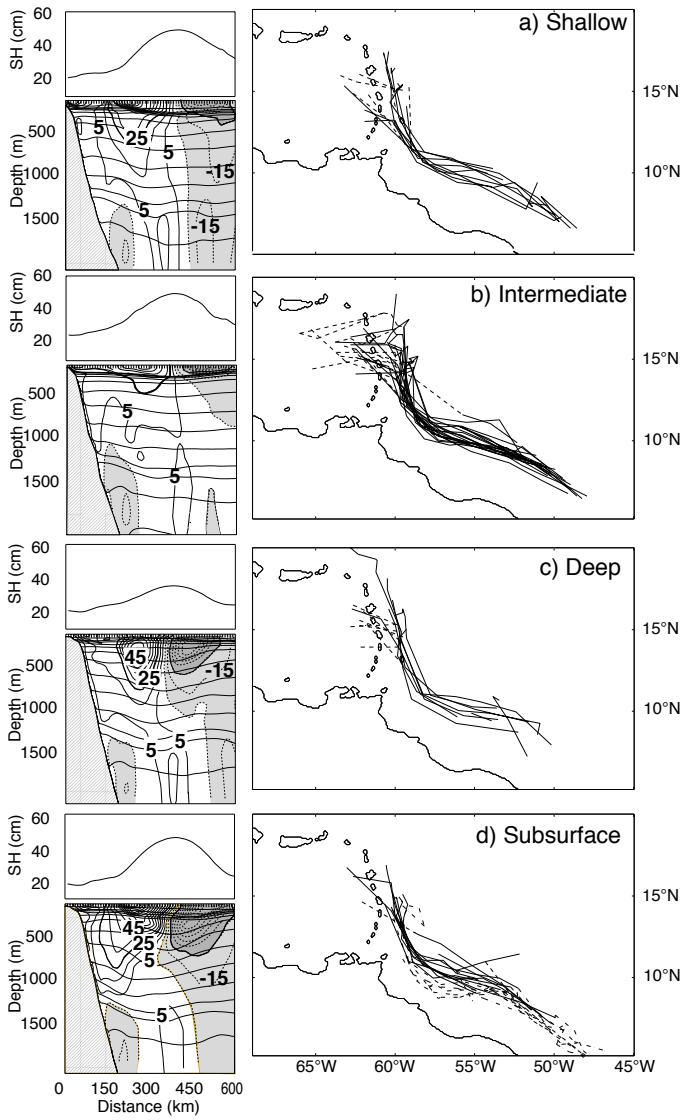

Figure 6. Sea surface height and vertical structure (velocity contours, cm/s, and isopycnic interfaces) for one ring of each type, and trajectories for all rings of the type, for: a) 'shallow' rings, b) 'intermediate', c) 'deep', d) 'subsurface'. Dashed lines indicate rings or anomalies after splitting or interacting with another ring or feature. 'Subsurface' rings not presenting a SSH signal are marked in dashed-dotted lines.

subtracting the time mean from the instantaneous SSH are about 12 cm for the subsurface rings and 15 to 25 cm for rings of other types. Thus the SSH signals of the modeled rings are generally stronger than those of the observed rings. Also, while the modeled subsurface rings show smaller SSH anomalies than the other types of rings, about 2/3 of the modeled subsurface rings are still detectable from the surface. This contrasts with the only observed subsurface ring (Wilson *et al.*, 2002), which showed a very small SSH anomaly. Whether this observed subsurface

Table 2
Ring type characteristics

	N	R(km)	σ_R (km)	N/yr	% enter Carib
shallow	8	114	17	1.3	37
intermediate	21	125	16	3.3	43
deep	7	130	23	1.2	14
subsurface	14	82	8	2.3	28
all	50			8.3	34 [1]

For each type of ring: number of rings during 6 model years, averaged radius of maximum velocity for the upper part of the ring, radius mean square deviation, number of rings per year, and percentage of rings of the type that move entirely into the Caribbean. Totals for rings of all types are also listed.
[1]: Percentage of rings of all types moving into the Caribbean (weighted average of the percentages for each type).

ring is typical of these types of features is unknown.

The number of rings of each type generated during the 6 model years is listed in Table 2, along with the upper average radius of maximum velocity and its standard deviation for each type, and the average number of rings per year. (The upper radius of maximum velocity is the average distance from the ring center to the maximum swirl velocity surrounding the center, in the upper part of the ring.) The mean ring radii of maximum velocity range from 115 to 130 km for the 'shallow', 'intermediate', and 'deep' types, with a standard deviation of 16 to 23 km. The averaged radius is smaller for the subsurface ring type, with a mean of 82 km and standard deviation of 8 km. This difference is consistent with the results of Wilson *et al.* (2002), who found an average radius of 150 km for the three surface intensified rings that they surveyed, and a smaller radius of 110 km for their subsurface ring. The actual modeled values appear to be somewhat smaller than observed, by O(20 km), regardless of ring type. However, Goni and Johns (2001) estimated the length scale of rings from altimeter-derived upper layer thickness maps, and found a smaller mean value of 95 km with a standard deviation of 25 km.

For some subsurface rings, the subsurface signal first appears near the equator (Figure 6 d), in the region of the subsurface NBC retroflection into the Equatorial Undercurrent (Figure 1). West of 50°W, the trajectories for different ring types are generally similar to each other in the region off the South American coast, but start to differ when the rings reach the Antilles. Some rings appear to enter the Caribbean nearly intact (shown by solid lines in Figure 6); others interact and merge with other rings or westward-propagating wavelike features, or a percentage of the ring separates and enters the Caribbean (dashed lines in Figure 6). Some rings stay to the east of the Antilles and move northward, where they either decay or merge with other features. The rings that enter the Caribbean, having diameters larger than the Lesser Antilles passage widths, generally go through several passages at the same time and recombine in the lee of the islands, a behavior noted in Simmons and Nof (2002). A larger percentage of shallow (37%)

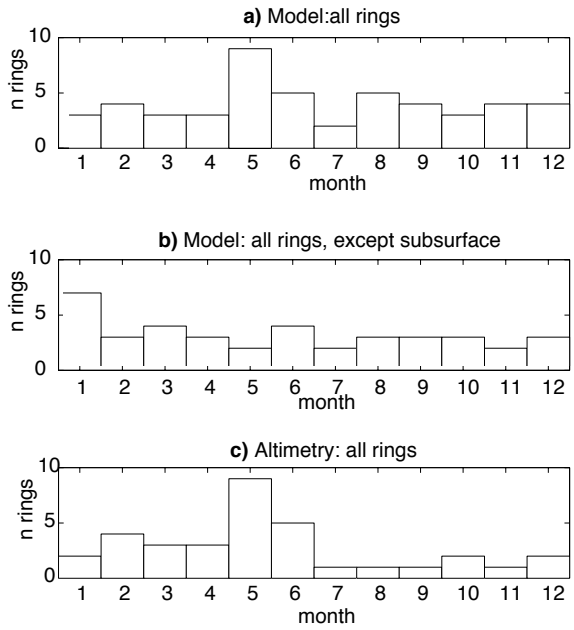

Figure 7. a) Number of rings generated as a function of the month of the year during 6 years, for all types of rings in the model; b) same as a) except subsurface rings are not included; c) same as b) obtained from TOPEX/Poseidon data.

and intermediate (43%) rings move into the Caribbean than do the deep (14%) and subsurface (28%) rings. This suggests that the deep and subsurface rings, having the deepest reaching velocity structures, tend to be more influenced by the island arc topography and are less able to penetrate into the Caribbean. In most cases, there is a northward burst in the rings' propagation speed as they approach the Antilles. The majority of the rings, characterized by their positive SSH anomalies with respect to the surroundings, move northward and pass near to or east of Barbados. As mentioned in section 4.2, the rings then stall for a while before entering the Caribbean Sea, the SSH anomaly increasing when rings merge. This in part explains the secondary maximum in SSH variability north of Barbados (Figure 5).

Figure 7a shows the number of rings of all types generated during the 6 model years as a function of the month in which they were formed. Rings are formed in all months of the year, but show the largest number formed in May and the minimum number formed in July. Since subsurface rings may not be detectable from the TOPEX/Poseidon SSH anomalies, Figure 7b also shows the distribution of modeled rings of the shallow, intermediate, and deep types only. This distribution can be compared to the similar figure derived from altimetry (Figure 7c). A total of 34 NBC rings were identified from 6 years of TOPEX/Poseidon data by Goni and Johns (2001), counting only the SSH anomalies that were clearly discernible by their amplitude. The number of modeled surface-intensified rings (*i.e.*, of the shallow, intermediate and deep types) generated during 6 years is 36, or 6 rings per year, in good agreement with the TOPEX/Poseidon observations (Table

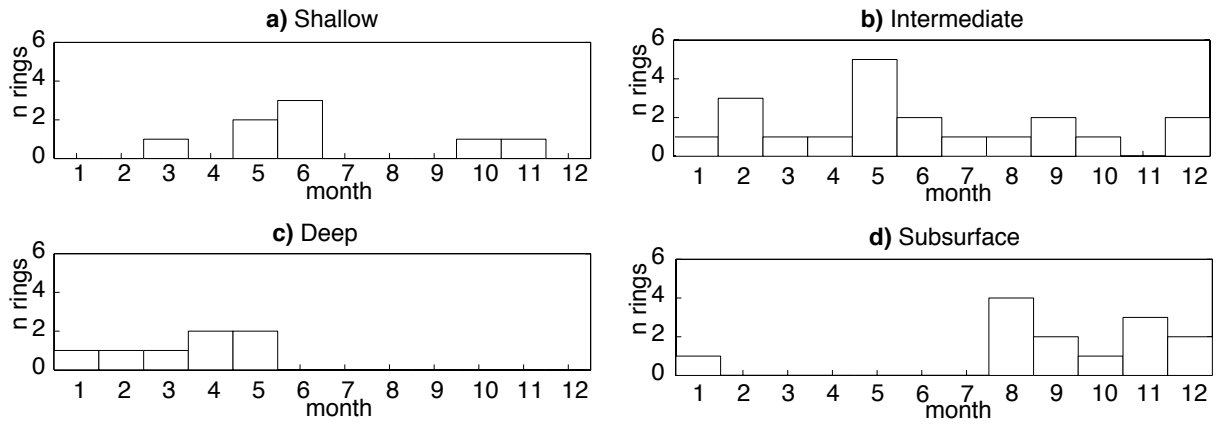

Figure 8. Number of modeled rings generated as a function of the month of the year during 6 years, for rings of each type: a) shallow, b) intermediate, c) deep, d) subsurface.

2). In the model, a maximum number of surface intensified rings are generated in spring/summer (May and June, Figure 7b), while in the observations the maximum occurs in winter (January) but with a less pronounced seasonal variation (Figure 7c).

The seasonal distribution of formation rate for each ring type is shown in Figure 8. Subsurface rings are generated in fall and early winter, while deep rings are generated in late winter and spring (with maximum generation in April and May). From June to December, the only rings with significant velocities below 700 m are the subsurface rings, which have a small surface signature. The shallow and intermediate rings can be formed throughout the year but have a maximum formation rate in late spring to early summer (May or June). A discussion of these differences will be presented in the last section of the paper.

Further analysis of the ring signal can be carried out from velocity time series. The time series of the north-south velocities at 10°N and 58°W are shown in Figure 9 for one model year, at the surface, for layer 6 ($\sigma_o = 26.52$, average depth 217 m) and for layer 9 ($\sigma_o = 27.22$, average depth 752 m). The reference point location was selected between the envelopes of the trajectories of rings with a surface signal and those with no surface signal; most of the trajectories pass just east of the reference location (see Figure 4a; the reference point is marked with a solid circle). These velocity time series show, for most cases, that there is a positive (northward) velocity when a ring approaches, and a drop to a negative value as the ring passes through the longitude of the reference point, with each rapid drop in the time series corresponding to the passage of a ring. Independently determined (from SSH maps for the rings with surface signal, and from subsurface maps otherwise) times for ring passage through the longitude of the reference location are marked by vertical lines, and the type of each ring is indicated.

As can be seen in Figure 9a, the surface velocity signatures of most of the modeled rings are very similar, but the shallow rings (e.g., August in Figure 9) decay

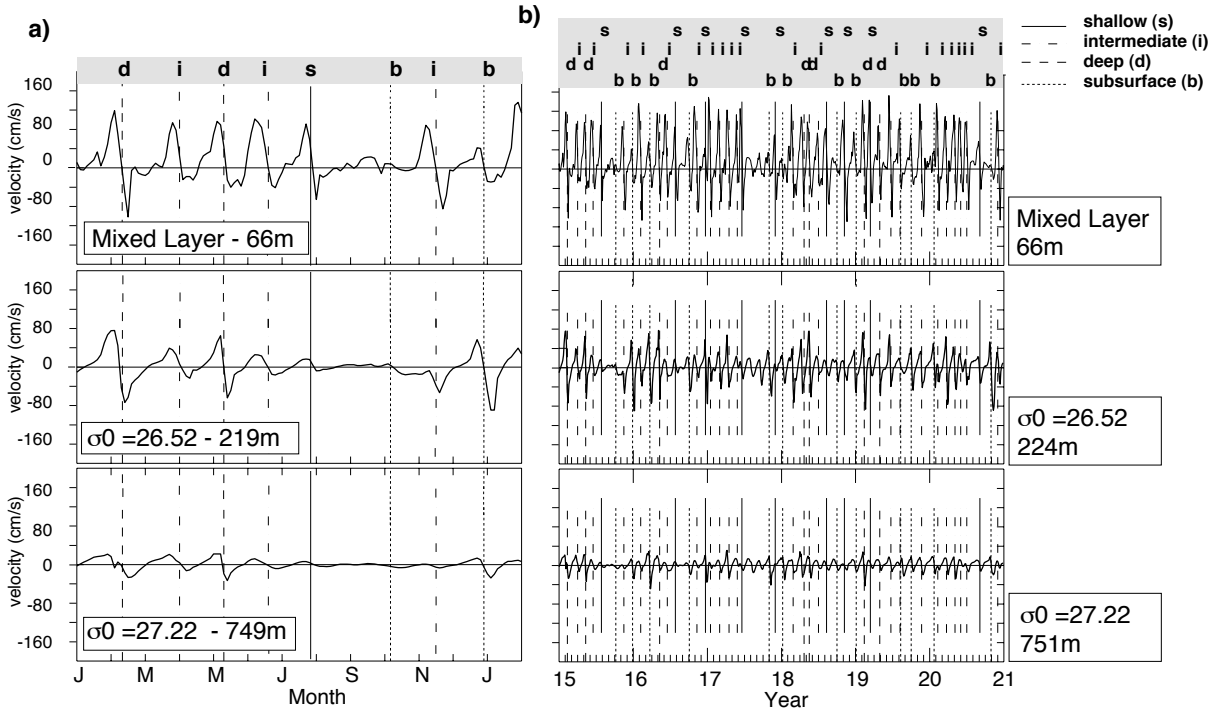

Figure 9. Time series of northward velocity for year 15, at 10°N 58°W, for the surface and for layers 6 and 9 (top, center and bottom panels). Given are the value of σ_0 and the time-mean depth at which the layer is located. Rings passing through 58°W are marked, as determined from SSH, velocity, and salinity. b: same for model years 15-20.

rapidly with depth when compared to the other types of rings. The deep rings (Feb. and May in Figure 9) predominate in deeper layers. The subsurface rings have generally a smaller surface velocity signal. The subsurface ring present in Dec.-Jan. shows a larger velocity in layer 6 than at the surface. A previous subsurface ring (October in Figure 9) is not apparent in the time series because the ring passes to the south-west of the reference location, not producing a significant signal there. (this is a ring with no SSH signal, indicated with a dashed-dotted trajectory in Figure 6). The velocity time series shows a quiet period around September, with smaller oscillations in the surface and subsurface meridional velocities than in other periods; this is also a period when no rings were independently identified from SSH. This quiet period is consistent with a minimum number of rings generated in July (Figure 7 b,c), since it takes about two months for the rings to arrive from the region of generation to the reference location at 10°N. In Figure 9b, the same velocity time series are shown for all 6 model years. Each large oscillation is associated with the passage of a NBC ring. Only a few rings (generally of the subsurface type) do not produce a velocity signal at the selected reference point; these are rings passing at a distance larger than the ring radius. The less active September period is present in all years, and is especially pronounced in some years (e.g,

year 17). It is important to note that the interannual variability in the model is independent from the forcing, since monthly climatological data are used to force the model.

4.4. Effect of NBC rings in the transports through the Lesser Antilles passages

As the rings reach the Lesser Antilles, observations indicate that they have a strong impact on the local water characteristics and circulation. For example, transport of entrained Amazon River water by North Brazil rings (Kelly *et al.*, 2000, Fratantoni and Glickson, 2002) influences larvae recruitment around Barbados (Cowen and Castro, 1994). Furthermore, North Brazil rings induce large variability in the transport between the passages through the Lesser Antilles (Johns *et al.*, 2003).

The modeled mass transports through the Lesser Antilles passages show energetic oscillations. Time series for the transport through three of the Lesser Antilles passages (Grenada Passage at 12°N, the southernmost passage; St. Lucia Passage at 14°N; and Dominica Passage at 15°N) are shown in Figure 10a. The circulation patterns (SSH contours and velocity vectors) corresponding to four days during the time of a particularly large variation in transport (May of year 15) are also shown in the figure. Positive transports correspond to flow entering the Caribbean. The transport through the southernmost passage diminishes from day 126 to 153 (Figure 10a) as a ring approaches the Antilles (Figures 10 b,c,d). This is due to the anticyclonic circulation associated with the ring, which diverts the flow near the passage northward (Figure 10 d,e) from its otherwise westward direction, resulting in a smaller transport. In this example, the ring moves toward the north, staying east of the Lesser Antilles. Farther north at St. Lucia and Dominica Passages, the decrease in transport occurs at successively later times (day 144 for St. Lucia, day 153 for Dominica). The cycle for the Dominica passage transport is particularly intense as this ring moves northward along the east side of the Lesser Antilles.

The next large transport variation in Grenada Passage occurs in June (Figure 10a) and corresponds to the next ring moving along the coast (seen in the lower right of Figure 10d), which induces a similar diversion of the flow. This ring partially enters the Caribbean through the southern passages (not shown), and the resulting amplitude variations in the transports through St. Lucia and Dominica passages have smaller amplitudes than those in March. The next transport oscillation in July-August (Figure 10 a) corresponds to a ring that enters the Caribbean between Grenada and St. Lucia passages (not shown), resulting in transport variability through Grenada and St. Lucia comparable to those in June. The transport fluctuations induced in the passages by the rings are of the same order as the mean transports through each of the passages.

5. TRANSPORT OF SOUTHERN ATLANTIC WATER BY RINGS

The contribution of NBC rings to the upper limb of the meridional overturning circulation in the Atlantic is still an open question. In particular, it is important to quantify how much water of southern hemisphere origin is transported north-

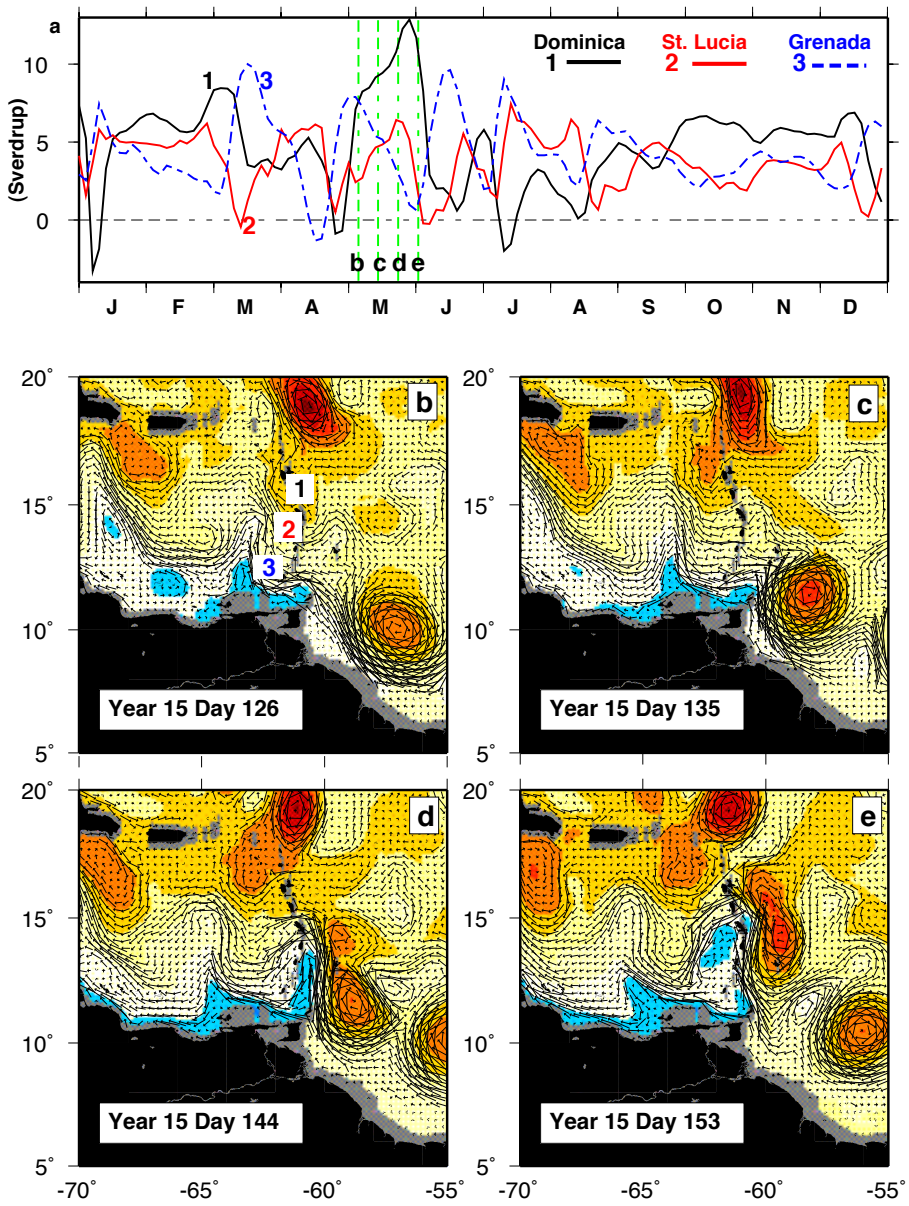

Figure 10. a) Time series of the transport through Lesser Antilles passages Grenada(1), St. Lucia(2) and Dominica(3); b),c),d),e): SSH (color coded from 0 to 70 cm, at 10 cm interval, blue to red) and velocity vectors at 4 days shown by vertical lines in a).

ward in the rings as compared to other pathways. In this section, we estimate the ring transport in two ways, by determining the volume of water inside the rings from their physical properties (their depth and diameter), and by calculating the proportion of southern water contained in the NBC rings through a detailed water mass analysis.

5.1. Transport from criteria on radius and vertical extent

We first present here the traditional approach of computing the geometric volume of the rings from the vertical and horizontal extent of the rings' velocity field. Consistent with Johns et al. (2003 - this issue), the volume of South Atlantic water that is trapped and transported within a ring is assumed to correspond to the portion of the ring that is nearly in solid-body rotation, which is from the center of the ring out to the radius of maximum azimuthal (swirl) velocity. For the following analysis, we use vertical sections of the ring meridional velocity at 10°N. In order to compute the ring volume, we consider the following criteria for the depth and radius of the rings: (1) the upper (for subsurface rings) and lower depth limits correspond to the locations where the swirl velocity drops below a minimum of 10 cm/s, and additionally the ring vertical extent is limited to layer 9 or above ($\sigma_o = 27.22$, about 800-900 m), thus eliminating contributions from below the main model depth of the South Atlantic intermediate water (salinity minimum in Figure 11 e), and (2) the ring radius is taken as the distance from the center of the ring to the maximum swirl velocity, with this distance (which can vary with depth in about 25% of the rings) being averaged azimuthally and over the total depth of the ring as defined above. We do not include any contribution to ring transport below layer 9 because those layers do not show a clear ring salinity signal arriving at 10°N (not shown).

The resulting ring volumes and other ring characteristics at 10°N are listed in Table 3 for all the rings identified during the six model years (year 15-20). The annualized transport associated with each ring is also shown, which is obtained by dividing the corresponding ring volume by the number of seconds in one year. According to this method, the resulting net transport by rings for the 6 year period is 6.6 Sv. It should be noted that in Table 3 there are only 49 rings crossing 10°N (one less than the total of 50 in Table 2), due to a merger of two sequential rings that took place in year 19 shortly after the rings were formed.

5.2. Transport from water mass analysis

An alternate way to determine the amount of South Atlantic water transported by the modeled rings is to specifically identify the South Atlantic waters according to their watermass properties. Waters of South Atlantic origin are characterized by lower salinity throughout the thermocline and intermediate layers than is seen in waters in the North tropical Atlantic on the same density surfaces. To illustrate this, we show in Figure 11 a,b maps of horizontal distribution of salinity at the surface and in layer 5 ($\sigma_0 = 26.18$, 19°C, 100 m) for a time when a ring is just being formed from the NBC retroflection (year 14 day 330). Signatures of the rings are evident in the subsurface layer (layer 5) north of the retroflection in Figure 11 b, one at 9°N and one interacting with the Lesser Antilles south of Barbados. We focus on the transport of this low salinity water from the equator northwards, and call it 'southern water', being the mixture of water of South Atlantic or equatorial origins that arrived at locations around the equator and 45°W. We call 'ambient water' the water present at the ring formation region that is not of South Atlantic and equatorial origins, i.e., the background water away from the NBC in the region

Table 3
Ring characteristics

	day	type	R velM	depth	V	transp v	
1	15.040	deep	150*	900	64	2.0	
2	15.085	interm	130	750	40	1.3	
3	15.120	deep	150	900	64	2.0	
4	15.160	interm	130	450	24	.8	
5	15.205	shallow	100	400	13	.4	
6	15.252[1]	subs	80	700	16	.4	
7	15.315	interm	105*	500	17	.5	
8	15.350	subs	95	750	21	.7	
						8.1 Sv	tot year 15
9	16.030	interm	120	750	34	1.1	
10	16.070	subs	80	800	16	.5	
11	16.128	deep	130	800	42	1.3	
12	16.165	interm	150	650	46	1.5	
13	16.205	shallow	120	400	18	.6	
14	16.272	subs	100	650	20	.6	
15	16.300	interm	130	400	21	.7	
16	16.345	subs	80	750	15	.5	
						6.7 Sv	tot year 16
17	17.030	interm	130	550	29	.9	
18	17.055	interm	120	700	32	1.0	
19	17.105	interm	130	850	45	1.4	
20	17.140	interm	105	700	24	.8	
21	17.155	shallow	130	200	11	.3	
22	17.246	subs	75	700	12	.4	
23	17.295	subs	90	700	18	.6	
24	17.325	shallow	90	150	4	.1	
25	17.357	subs	80	850	17	.5	
						6.1 Sv	tot year 17
26	18.045	interm	120	750	34	1.1	
27	18.110	deep	105	850	29	.9	
28	18.130	deep	120*	900	41	1.3	
29	18.180	interm	160*	700	56	1.8	
30	18.210	shallow	120	300	14	.4	
31	18.267	subs	75	700	12	.4	
32	18.300	shallow	120	500	23	.7	
33	18.351	subs	80	500	10	.3	
						6.9 Sv	tot year 18
34	19.035	deep	100*	850	27	.8	
35	19.070	shallow	105	400	14	.4	
36	19.110	deep	80*	850	17	.5	
37	19.160	interm	120*	750	34	1.1	
38	19.213	interm	100	700	22	.7	
39	19.270	subs	90*	550	14	.4	
40	19.315	interm	110*	800	30	1.0	
						4.9 Sv	tot year 19
41	20.015	subs	80	800	16	.5	
42	20.030	interm	130	350	19	.6	
43	20.075	interm	120	750	34	1.1	
44	20.120	interm	120	700	32	1	
45	20.140	interm	105	750	26	.8	
46	20.180	interm	150	300	21	.7	
47	20.225	shallow	130	500	26	.8	
48	20.300	subs	80	700	14	.4	
49	20.315	interm	120	600	27	.9	
						6.8 Sv	tot year 20

Ring number, date in which the ring is at 10°N, type of ring, radius of maximum velocity (km), depth-averaged radius, ring volume obtained with the ring depth and radius ($10^6 m^3$), and annualized ring volume transport (Sv).

* Depth average radius of max vel different from upper radius. [1] Day and transport at 9°N.

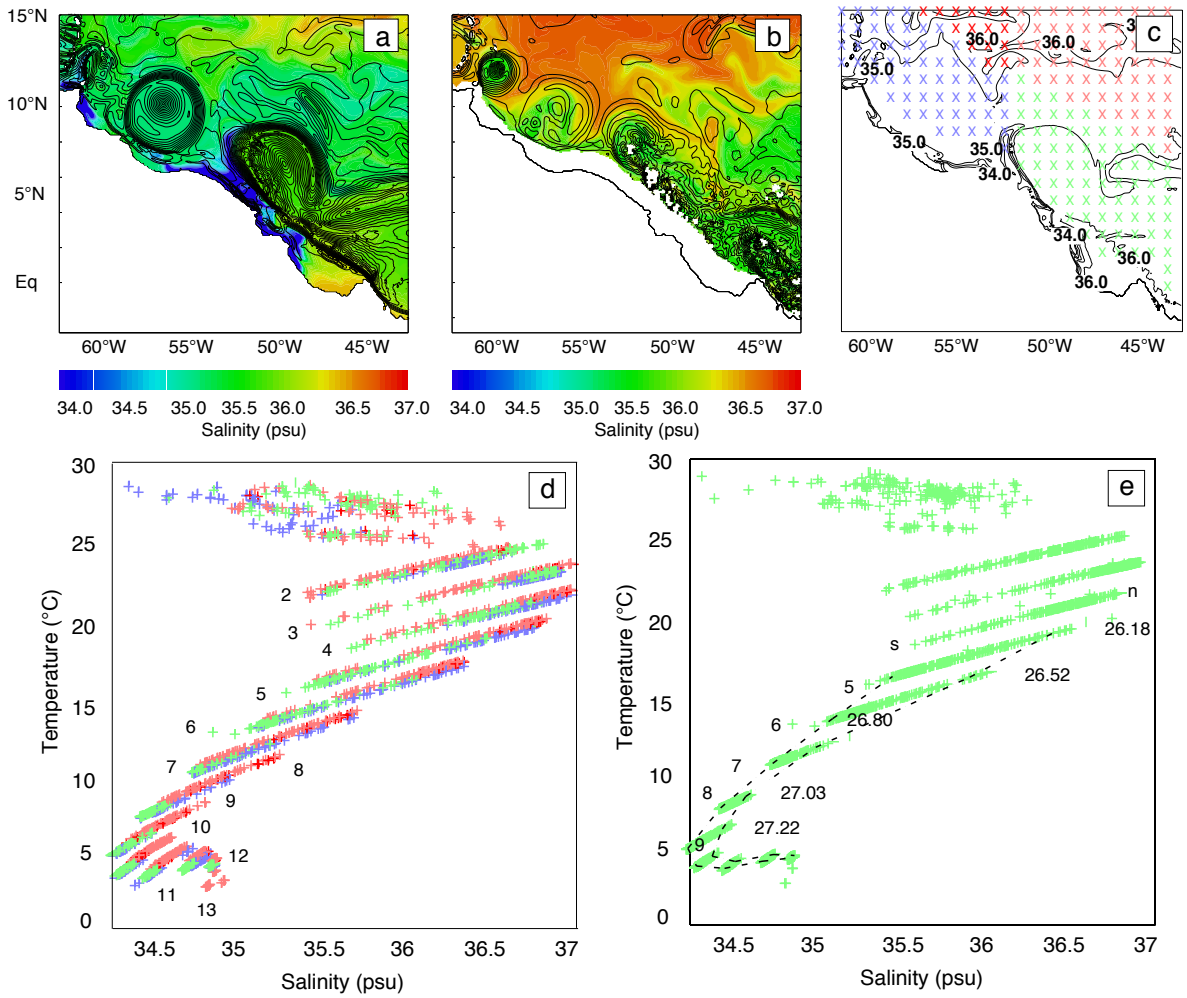

Figure 11. a) Surface and b) subsurface ($\sigma_0 = 26.18$) salinity for a day on which a ring is being generated (model year 14, day 330). c) map of locations in 4 subdomains, east (green) and west (blue) of $52°$W in a region parallel to the coast containing the North Brazil Current and rings; east (pink) and west (red) of $52°$W between the previous regions and $15°$N (surface salinity contours indicated; year 14 day 330). d) TS diagrams for locations over the regions, each TS value is indicated with a + sign with color according to location as in c). Layer numbers are indicated; data from 3 model dates are included (day 330 of year 14, days 33 and 210 of year 15). e) TS diagrams for points in the southeast region (corresponding to the region of green crosses in c)) and reference profiles for 'southern' and 'northern' water (dashed lines labeled s and n, with low and high salinity respectively, layers 5-9). Same dates as in d). Density values and layer numbers are indicated.

of ring formation. At the surface (Figure 11 a), water from the south is actually saltier than water near the eastern Antilles, the horizontal salinity gradient being reversed with respect to the subsurface (layer 5). This is due to excess precipitation along the latitudes of the ITCZ and to input of fresh Amazon river water. The river water is partially entrained in the rings periphery and can move offshore between

rings.

The model T-S diagram for the region is shown in Figure 11 d, with colors indicating 4 regions as shown in Figure 11 c, for the same model date as in Figure 11 a,b. The T-S diagram shows that for the surface to layer 4 (σ_0=25.77), a distinct characteristic in the salinity signal can not be defined for each of the regions, and therefore it is not possible to identify from the diagram the origin of the modeled water masses. This is mainly due to the inversion of the horizontal salinity gradient with respect to that of the layers below, resulting from precipitation and Amazon river water induced-mixing. For model layers 5 through 9 (σ_0 between 26.18 and 27.22), which correspond to waters below the subsurface salinity maximum and above the intermediate water salinity minimum, it is apparent in the T-S diagram that the green region (hereafter referred to as the 'incoming region') has fresher salinity than the rest of the domain (Figure 11 d). We define 'southern water' ('ambient water') as the waters with lowest (highest) salinities for each layer in the incoming region. Reference T-S profiles (Figure 11 e) for 'southern water' and for 'ambient water' for layers 5 to 9 are then constructed by averaging the 10% lowest and highest salinities for each isopycnic layer in the incoming region for data from 3 different model dates (day 330 of year 14, days 33 and 210 of year 15) and obtaining the corresponding temperature from the layer density. The percentage of southern water inside a ring is then calculated by linearly interpolating in distance to the southern and ambient water profiles in T-S space:

$$\alpha = \frac{\sqrt{(T-T_s)^2+(S-S_s)^2}}{\sqrt{(T-T_s)^2+(S-S_s)^2}+\sqrt{(T_n-T)^2+(S_n-S)^2}},$$

where T, S, T_s, T_n, S_s, S_n are the temperature (salinity) of the point and those of the southern and ambient water reference profiles at the selected density, and the percentage of southern water is $\alpha \times 100$. Percentages 0 and 100% were assigned to points with $S < S_n$ and $S > S_s$, respectively. Since the density isolines are close to linear, as seen in Figures 11 d,e, we found no significant difference in the results if the interpolation was instead done in either T or S alone.

The volume of southern water carried by the ring between layers 5 and 9 was computed by integrating α over the volume of the ring. The volume of the ring is defined slightly differently than in section 5.1 and can include waters outside the radius of maximum velocity. The contributing layers were selected from horizontal maps and animations of salinity and southern water percentage. The horizontal areas of integration were chosen for each layer from the animations as the area trapped and advected by the ring. The total volume of southern water for layers 5-9 was then obtained by adding the grid volume multiplied by α (percentage of southern water divided by 100) over the contributing grid points. For the surface intensified rings, the volume for layers 1-4 ($\approx$ upper 150 meters) enclosed by the radius of maximum velocity was added to the water mass derived volume to give the total southern water volume.

We illustrate this process by looking in more detail at rings in year 15. The percentage of southern water in layer 5 and below is shown in Figure 12 a for a

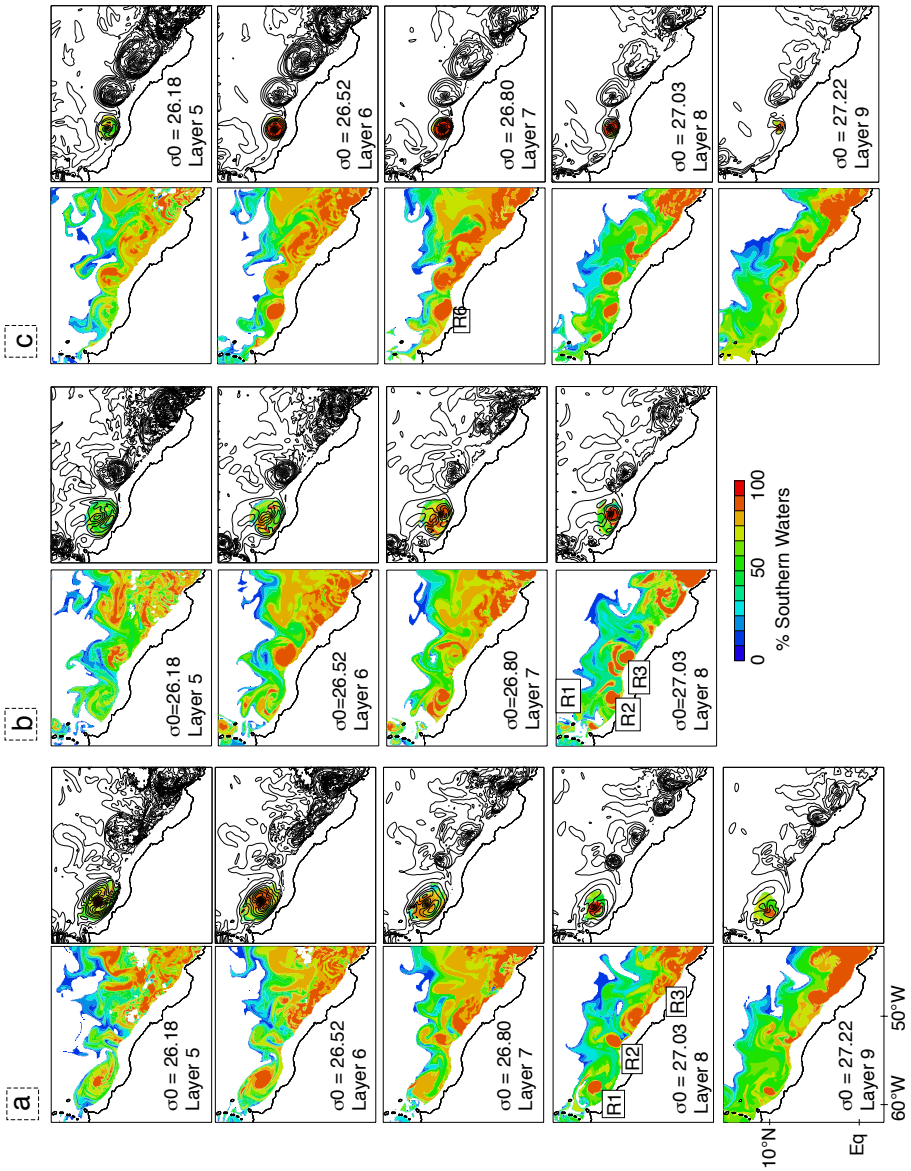

Figure 12. a)Percentage of southern water in ring 1 of the deep type, layers 5-9 (left panels), and the same quantity in the region contributing to ring transport (right panels), together with velocity magnitude contours (contour interval 10 cm/s). Model date is year 15 day 33. Ring 1, two features that merge into ring 2, and ring 3, are indicated at layer 8 (R1, R2, R3). b) Same for ring 2 of the intermediate type, layers 5-8, model year 15 day 84. c) Same for ring 6 of the subsurface type, at year 15 day 252.

large ring centered at 10°N, 57°W, at year 15, day 33, which was generated just after the state shown in Figure 11 a,b. This ring (Figure 12 a, ring 1) is of the deep type and is the result of the merging of two smaller rings at previous times (it was counted as one ring in Table 2). It follows the trajectory in Figure 6c reaching 20°N east of the Lesser Antilles. For this ring, the southern water percentage has

Table 4
Water mass characteristics of the rings during year 15

	day	type	layer	vol	transp	transp kin
1	15.040	deep	9	66	2.1	2.0
2	15.085	interm	8	44	1.4	1.3
3	15.120	deep	9	60	1.9	2.0
4	15.160	interm	7	25	.8	.8
5	15.205	shallow+subs	6,8	16	.5	.4
6	15.252[1]	subs	3-8	22	.7	.4
7	15.315	interm	8	19	.6	.5
8	15.350	subs	3-9	32	1.0	.7
					9.0 Sv tot year 15	8.1 Sv

Ring number; date in which the ring is at 10°N (except [1] at 9°N); ring type; deeper ring layer (surface intensified rings) or upper and deeper ring layers (subsurface rings); volume of southern water ($10^6 m^3$); annualized ring transport of southern water (Sv); for comparison, ring volume from kinematic considerations as in Table 3.

relatively high values in regions extending beyond the radius of maximum velocity. Southern water percentage maps at later times (not shown) indicate that some areas with relatively high southern water content on the perimeter of the ring in layer 8 do not move with the ring (these areas were not included in the volume estimate).

The percentage of southern water for a ring of intermediate type is shown in Figure 12 b, for year 15, day 84 (ring 2). This ring clearly has higher southern water percentage in the lower thermocline and upper intermediate layers (layers 7 and 8). Layers above (5 and 6) show a strong mixing of southern and ambient waters in the ring core, indicating a vigorous interleaving process in the rings that can lead to a complex vertical distribution of southern water transported by the rings. In the deeper layers, the ring resulted from the merging of two features that at day 33 were at 53°W (showing no surface signal) and 49°W (see Figure 12 b, layers 7 and 8). At later times, ring 2 follows a trajectory entering into the Caribbean through the mid Lesser Antilles passages. Also seen in Figure 12 b are two rings of the deep type: ring 1 (already discussed) at 14°N just to the east of the Lesser Antilles, and ring 3 at 52°W. Ring 3 shows a core with very high southern water percentage in layers 5,6 and 8,9 (layer 9 not shown), but in layer 7 the core had a lower value, showing the complexity of the vertical coupling between the thermocline and the upper intermediate layers. Due to this low core in layer 7, the transport determined by the water mass method is slightly smaller than the value estimated by the kinematic method.

A ring of the subsurface type is shown in Figure 12 c, at year 15, day 252 (ring 6). For this ring, the maximum velocity occurs in layer 6 (at about 200 m), the southern water percentage is a maximum in layers 6-8, and the velocity isolines

Table 5
Estimation of water mass transport for all rings

	n	transp	avg T per ring	fact	transp wm
shallow	8	.6	.48	1.	.6
interm	21	3.4	.98	1.1	3.7
deep	7	1.5	1.28	1.0	1.5
subs	13	1.1	.49	1.5	1.7
6 years	tot 49	avg 6.6 Sv			avg 7.5 Sv

Estimation of water mass transport by renormalization of the kinematic transport according to the one year water mass results. The table lists type of ring; number of rings during the 6 model years; average annualized transport over the 6 years; average annualized transport per ring; factor to convert to water mass transport; total estimated water mass transport by all rings of the type, renormalized to one year ($\frac{transp \times fact}{6}$). Last row: totals or averages for the 6 model years.

follow closely the sharply defined core of southern water.

Due to mixing and diffusion, regions with anticyclonic motion in the periphery of the rings can have a relatively high southern water percentage, but do not necessarily move with the ring. The water mass calculation is laborious and, consequently, was done for only one model year (year 15). This year was chosen because it has the maximum number of rings and because at least one ring of each class was represented. The results are shown in Table 4. A total transport of 9 Sv of southern water was thus obtained for year 15.

5.3. Comparison of kinematic and water mass methods

The ring transports for year 15 obtained from both methods are listed for comparison purposes in Table 4. The total of 9 Sv obtained for that year with the water mass method is about 11% higher than the 8.1 Sv obtained with the kinematic method. Averaging the transports for each ring type, the differences between the water mass and kinematic method transports are about 12% for the intermediate rings, 0% for the deep rings, and 50% for the subsurface rings. The transports of the shallow rings are identical, by definition, for both methods. The results are listed in Table 5 (5th column), showing for each ring type the ratio between the average ring transports by the water mass and kinematic methods, as obtained from all rings of year 15. The subsurface rings show a larger difference between the two methods, attributable to the fact that they tend to have a high southern water percentage extending farther from the radius of maximum velocity. For the other ring types, the southern water percentage has generally already decreased substantially from its core value at the radius of maximum velocity.

Assuming that this comparison is representative, we now use the results of year 15 to estimate the southern water transport by rings in the remaining 5 years (years 16-20). The estimated water mass transport for each ring is obtained by scaling the kinematic method transport with the factor (ratio) corresponding to

Table 6
Transport of southern water by rings and mean meridional transport

year	Transp SW	MT
15	9.2	17.0
16	7.9	16.7
17	7.2	17.9
18	7.7	17.4
19	5.6	17.0
20	7.8	17.5
avg	7.5 Sv	17.3 Sv

For each year, estimated transport of southern water by rings, and annual mean meridional transport over the whole Atlantic from the surface to σ_0=27.22 (layer 9), at 5°N.

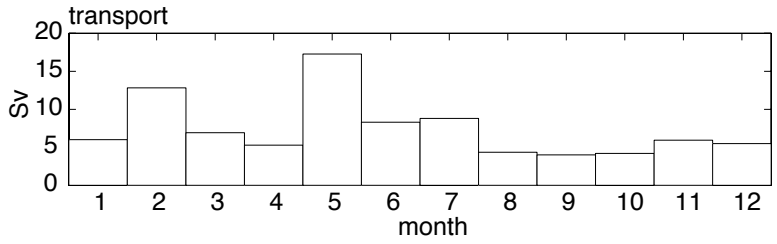

Figure 13. Monthly distribution of the transport of southern water by rings at 10°N. The transport average is the 7.5 Sv obtained for the ring transport. (The annualized ring transport for each month was multiplied by 12.)

each ring type described above. This results in an estimation of 7.5 Sv of southern water carried by the rings at 10°N, for years 15-20 (Table 6). The difference between the two methods is on the order of 15%. Of these 7.5 Sv, we estimate that the upper 300 m transported by rings is 2.6 Sv.

The same scaling is applied to obtain the monthly transport of southern water at 10°N averaged over the 6 years. Results are shown in Figure 13. The transport peaks during May due to deep and intermediate rings arriving at 10°N (see Figure 8), is small during August, September, October (during the period of low ring activity at that latitude), and is large in February due to intermediate and deep rings. The monthly distribution of southern water transport has a more pronounced variation than the monthly distribution of the number of generated rings of Figure 7a, due to the predominance of intermediate and deep ring generation during the first half of the year, which transport a larger volume of southern water than rings of shallow and subsurface type (see Figure 8).

6. DISCUSSION AND CONCLUSIONS

Results from a very high resolution North Atlantic simulation with the Miami Isopycnic Coordinate Ocean Model are analyzed and compared with published observations for the North Brazil Current and rings. The modeled mean and seasonal surface circulations show a good qualitative agreement with observations. The largest difference occurs for the NBC retroflection into the NECC in summer and fall: in the model 8 Sv continue westward of 48°W while observations suggest a complete retroflection, and the modeled NECC eastward flow is 15 Sv, 4 Sv weaker than observed. The excess NBC transport can be related to the model's relatively high meridional transport (about 3-5 Sv more intense than observed), while the weakness of the NECC could in part be attributable to the COADS climatological wind forcing.

The model generates a variety of rings (which we classify as shallow, intermediate, deep, and subsurface), in an average of 8.3 rings of all types per year, of which 6 are surface-intensified, in good agreement with the altimetry-derived 5.7 rings per year (Goni and Johns, 2001). The modeled rings are generated in all seasons, with maximum ring activity in May and minimum activity in July. Surface intensified rings, with maximum velocity at the surface and depths between 200 and 900 m, are generated with a maximum in May and June and a minimum in the rest of the summer and fall. Rings of the subsurface type, with maximum velocity signal in the subsurface layers, are generated at an average rate of about 2 per year. They are smaller in size and have a larger percentage of southern water associated with them than rings of other types. Deep and subsurface rings are generated in non-overlapping seasons. Deep rings occur in winter and spring. Subsurface rings are generated in summer and fall, when the number of surface intensified rings is smaller, alternating with rings of the intermediate type. In winter, when the deep rings start to be generated, the incoming NBC at 44°W has a slightly greater intensity and larger vertical velocity gradient surface-500 m than in other seasons; the deep rings are also generated in the spring near the location of the subsurface retroflection into the NECC, at a time when the subsurface retroflections into the EU and the NECC are closer. Some subsurface rings result from the detachment of the deep part of a ring of the intermediate or deep type; the subsurface ring then moves more slowly and can merge with a successive ring, showing the complexity in the vertical coupling between the upper and lower layers.

Surface intensified rings are mostly generated in the NBC surface retroflection region at latitude $\sim 7°$N. Subsurface rings originate in two regions: the first one near or to the south of the subsurface retroflection of the NBC into the EUC, at $\sim 3°$N, and the second one near the surface NBC retroflection, at $\sim 7°$N. The two regions of ring generation are similar to those found by Barnier *et al.* (2001). About 40% of the subsurface rings did not show any surface signal, some of them traveling at slower speed and nearer to the South American coast than rings of other types.

Several dynamic studies seem to be relevant to the ring generation mechanisms operating in the model. Da Silveira *et al.* (1999) produced a meandering NBC retroflection, with their equivalent barotropic piecewise constant vorticity formula-

tion for the convergence of the northward flowing NBC with the weaker soutward flowing NEC in the presence of a westward tilted coast. Ma (1996) showed that NBC rings can be generated either as a consequence of the reflection of westward propagating equatorial Rossby wave packets deepening the thermocline, or during the spin up by wind forcing. Jochum and Malanotte-Rizzoli (2003) proposed independent formation mechanisms for shallow and subsurface rings. In their model, surface rings are produced by reflection of Rossby waves generated by an unstable NECC on the North Brazil coast. Subthermocline and intermediate water rings are generated by a different process, in which an intermediate western boundary current crossing the equator breaks down into vortices due to the presence of a thin boundary layer unable to provide, by friction, the necessary change in potential vorticity. Deep rings are interpreted as the merger of a surface ring with one of the intermediate rings. In our model, this type of generation for deep rings is indeed observed. At the intermediate water layers (σ_0 = 27.03 or 27.22), the flow breaks into rings with smaller radius than that of the surface rings, at latitudes ranging from the equator to 5°N. Some of the modeled deep rings originate with a ring in the intermediate water layers, which later merges with a surface ring.

The interaction between upper and lower flow in ring formation is reminiscent of the mechanisms proposed by Cherubin (2000). As in their study, nonlinear destabilization of the upper layer retroflection front by a lower layer vortex allows subsurface rings generated near the equator to acquire a surface signal when reaching latitudes of the surface retroflection.

The model results show that ring formation processes in the NBC region are very complex, involving several processes and interactions between layers from the surface to the intermediate water. The formation of ring 1 of the deep type (formation stage shown in Figure 11 a,b, at 10°N in Figure 12 a) involves a subsurface ring that acquired a surface signal at the surface retroflection, shortly followed by the detachment of a surface ring, advancing faster than the subsurface ring, merging, and forming the deep ring. The vertical dependence in the southern water content for this ring further indicates that the ring was formed by the merging of vertically separated ring signatures. For ring 3 of the deep type, the surface and subsurface fronts and an intermediate layer ring are initially aligned vertically. The subsurface front first follows the surface front, then couples with the intermediate ring and detaches, with all layers moving together but the surface detaching last. Ring 11 of the deep type is generated at the end of the winter before the surface retroflection disappears. Its formation starts with two surface signals formed at the retroflection, which merge on top of the next subsurface ring signature to form the deep ring. The results also suggest that further dynamic studies are needed to fully understand the mechanisms for the formation of the variety of rings present in the region.

A major focus of this paper was on the determination of the amount of southern water that modeled rings trap and transport in their cores. The transport of water of southern origin by rings was estimated by integrating the southern water present in a region around the rings core that extends farther than the radius of maximum velocity. This resulted in an average value of 7.5 Sv of southern water

transported by rings of all types, or ∼40% of the 17.3 Sv total meridional transport from the surface to the intermediate water layers ($\sigma_0 = 27.22$, layer 9, mean depth $\sim$ 800 m). The southern water transported by the rings shows a complex vertical distribution, sometimes being contained in different percentages in the rings' subsurface and deep layers. The ring transport for individual years varied from 5.5 Sv to 9 Sv, even though the model was forced with seasonal climatological fields with no interannual variability. The annual mean zonally integrated meridional transport in the model also varies from year to year (Table 6). The transport of southern water by rings varies between 30% and 55% of the total meridional transport for $\sigma_0 \leq 27.22$ for the 6 model years. Since most of the annual mean modeled meridional transport occurs in the western boundary, this is also the approximate relation between the transport by rings and the total western boundary transport. There is no obvious correlation between ring transport and total MOC transport in the 6 years analyzed at time scales of 1-2 years. However, results from a similar simulation that had a 40% higher overturning gave about 1.5 more rings per year of the surface intensified types (about 25% increase), suggesting that the number of rings is in part influenced by the MOC. According to Schmitz (1996), the upper branch of the MOC consists of 14 Sv of upper ocean water, with the return flow of 18 Sv of North Atlantic Deep Water balanced by the upper branch plus the deep flow of Antarctic Bottom Water. The model upper and intermediate meridional transport is more intense (3 and 5 Sv) than the observed upper branch and NADW values. It is therefore possible that the model slightly overestimates the ring transport of southern water, the extra ring activity being related to the higher MOC.

The results confirm the complexity and importance of the North Brazil rings for the Atlantic interhemispheric transport of water. The agreement of these results with recent experimental ones presented by Johns *et al.* (2003) makes the present model suitable for further studies on ring generation processes and transport characteristics that cannot be accomplished by the use of observational data alone.

Acknowledgments

The authors want to thank F. Schott and C. Rooth for discussions, R. Zantopp for comments and help in technical aspects, L. Smith for her careful reading of the manuscript, and two anonymous reviewers for their comments. This research was supported by NSF grants OCE-9531852 and ATM-9905210, and by NOAA/AOML. Computations were performed on the Department of Defense (DoD) computers at the Stennis Space Center under a challenge grant from the DoD High Performance Computer Modernization Office.

REFERENCES

Arnault, S. and C.Le Provost. Regional identification in the tropical Atlantic Ocean of residual tide errors from an empirical orthogonal function analysis of TOPEX/POSEIDON altimetric data. *J. Geophys. Res.*, **102**, 21011-21036, 1997.

Barnier, B., T. Reynaud, A. Beckmann, C. Boning, J-M Molines, S. Barnard, and Y. Jia. On the seasonal variability and eddies in the North Brazil current: insight from model intercomparison experiments. *J. Progress in Oceanogr.*, **44**, 195-230, 2001.

Bleck, R., C. Rooth, D. Hu, and L.T. Smith. Salinity-driven thermocline transients in a wind- and thermohaline-forced isopycnic coordinate model of the North Atlantic. *J. Phys. Oceanogr.*, **22**, 1486-1505, 1992.

Bleck, R. and E. Chassignet. Simulating the oceanic circulation with isopycnic-coordinate models. In: Majundar, S.K. (Ed.), The Oceans: Physical-Chemical Dynamics and Human Impact, 17-39, 1994.

Borstad, G.A.. The influence of the meandering of the Guiana Current and Amazon River discharge on surface salinity near Barbados. *J. Mar. Res.*, **40**, 421-434, 1982

Bourles, B., Y. Goriou and R. Chuchla. On the circulation in the upper layer of the western equatorial Atlantic. *J. Geophys. Res.*, **104**, C9, 21151-21170, 1999 a.

Bourles, B., R.L. Molinari, E. Johns, W.D. Wilson and K.D. Leaman. Upper layer currents in the western tropical North Atlantic (1989-1991). *J. Geophys. Res.*, **104**, C1, 1361-1375, 1999 b.

Bracco, A., E.P. Chassignet, Z.D. Garraffo, and A. Provenzale. Lagrangian velocity distributions in a high-resolution numerical simulation of the North Atlantic. *J. Atmos. Ocean Tech.*, in press, 2003.

Candela, J., R.C. Beardsley and R. Limeburner, 1992. Separation of tidal and subtidal currents in ship mounted acoustic Doppler current profiler (ADCP) observations. *J. Geophys. Res.*, **97** (C1), 769-788, 1992.

Carton, J.A. and Y. Chao. Caribbean Sea eddies from TOPEX/POSEIDON altimetry and a $1/6^\circ$ Atlantic Ocean model simulation. *J. Geophys. Res.*, **104** (C4), 7743-7752, 1999.

Chassignet, E.P., L.T. Smith, R. Bleck, and F.O. Bryan. A model comparison: Numerical simulations of the North and Equatorial Atlantic oceanic circulation in depth and isopycnic coordinates. *J. Phys. Oceanogr.*, **26**, 1849-1867, 1996.

Chassignet, E.P., and Z.D. Garraffo. Viscosity parameterization and the Gulf Stream separation. In "From Stirring to Mixing in a Stratified Ocean". Proceedings 'Aha Huliko'a Hawaiian Winter Workshop. U. of Hawaii. January 15-19, 2001. P. Muller and D. Henderson, Eds., 37-41, 2001.

Cherubin, L. Descriptive analysis of the hydrology and mixing of the Mediterranean outflow and effects of topography on the stability of the Mediterranean undercurrents. Ph.D thesis, Universite de la Mediterranee, Centre d'Oceanologie de Marseille, 343pp, 2000.

Csanady, G.T.. A zero potential vorticity model of the North Brazilian Coastal Current. *J. Mar. Res.*, **43**, 553-579, 1985.

Cowen, R. K., and L.R. Castro. Relation of coral reef fish larval distributions to island scale circulation around Barbados, West Indies. *Bull. Mar. Sci.*, **54**, 228-244, 1994.

da Silva, A.M, C.C. Young, and S. Levitus. Atlas of surface marine data 1994. Technical Report. National Oceanic and Atmospheric Administration, 1994.

da Silveira, I.C.A., G.R. Flierl, and W.S. Brown. Dynamics of separating western boundary currents. *J. Phys. Oceanogr.*, **29**, 119-144, 1999.

Didden, N. and F. Schott. Eddies in the North Brazil Current retroflection region observed by Geosat altimetry. *J. Geophys. Res.*, **98**, 20,121-20,131, 1993.

Fratantoni, D.M., W.E. Johns and T.L. Townsend. Rings of the North Brazil Current: their structure and behavior inferred from observations and a numerical simulation. *J. Geophys. Res.*, **C6**, 10,633-10,654, 1995.

Fratantoni, D.M. and D. Glickson. North Brazil Current ring generation and evolution observed with SeaWiFS, *J. Phys. Oceanogr.*, **32**, 1058-1074, 2002.

Garraffo, Z.D., A.J. Mariano, A. Griffa, C. Veneziani and E.P. Chassignet. Lagrangian data in a high-resolution numerical simulation of the North Atlantic. I. Comparison with in-situ drifter data. *J. Mar. Syst.*, **29**, 157-176, 2001 a.

Garraffo, Z.D., A. Griffa, A.J. Mariano and E.P. Chassignet. Lagrangian data in a high-resolution numerical simulation of the North Atlantic. II. On the pseudo-Eulerian averaging of Lagrangian data. *J. Mar. Syst.*, **29**, 177-200, 2001 b.

Garzoli, S.L. and E.J. Katz. The forced annual reversal of the North Atlantic Equatorial Countercurrent. *J. Phys. Oceanogr.* **13**, 2082-2090, 1993.

Goni, G.J., and W.E. Johns. A census of North Brazil current rings observed from TOPEX/Poseidon altimetry: 1992-1998. *Geophys. Res. Lett.*, **28**, 1-4, 2001.

Gordon, A.. Interocean exchange of thermocline water. *J. Geophys. Res.*, **91**, 5037-5046, 1986.

Gordon, A., R.F. Weiss, W.M. Smethie Jr, and M.J. Warner. Thermocline and intermediate water communication between the South Atlantic and Indian Oceans. *J. Geophys. Res.*, **97**, 7223-7240, 1992.

Johns, W.E, S.L. Garzoli and G.J. Goni. Cross-gyre watermass transport by North Brazil Current Rings. In Interhermispheric Water Exchange in the Atlantic Ocean, Elsevier Oceanographic series, this volume, 2003.

Johns, W.E., T.N. Lee, F.A. Schott, R.J. Zantopp and R.H. Evans. The North Brazil Current retroflection: seasonal structure and eddy variability. *J. Geophys. Res.*, **95** (C12), 22,103-22,120, 1990.

Johns, W.E., T.N. Lee, R.C. Beardsley, J. Candela, R. Limeburner and B. Castro. Annual cycle and variability of the North Brazil Current, *J. Phys. Oceanogr.* **28**, 103-128, 1998.

Johns, W.E, T.L. Townsend, D.M. Fratantoni, W.D. Wilson. On the Atlantic inflow to the Caribbean Sea. Deep Sea Research, **I 49**, 211-243, 2002.

Jochum, M. and P. Malanotte-Rizzoli. On the generation and importance of North Brazil Current rings, *J. Mar. Res.*, **61**, 147-162, 2003.

Katz, E.J.. An interannual study of the Atlantic North Equatorial Countercurrent. *J. Phys. Oceanogr.*, **23**, 116-123, 1993.

Kelly, P., Lwiza, R. Cowen and G. Goni. Low-salinity Lenses at Barbados, West Indies: Their Origin, Frequency and Variability. *J. Geophys. Res.*, **105**, 19699-19708, 2000.

Kraus, E.B. and J.S. Turner. A one-dimensional model of the seasonal thermocline: II. The general theory and its consequences. Tellus, **19**, 98-106, 1967.

Larsen, J.C.. Transport and heat flux of the Florida Current at 27°N derived from cross-stream voltages and profiling data: Theory and observations. Phil. Trans. of the Royal Society of London, 338, 169-236, 1992.

Levitus, S.. Climatological Atlas of the World Ocean. NOAA Professional Paper 13, US Dept of Commerce, NOAA, 1982.

Ma, H.. The dynamics of North Brazil Current retroflection eddies. *J. Mar. Res.*, **54**, 35-53, 1996.

Mayer, D.A. and R.H. Weisberg. A description of COADS surface meteorological fields and the implied Sverdrup transports for the Atlantic Ocean from 30°S to 60°N. *J. Phys. Oceanogr.*, **23**, 2201-2221, 1993.

Murphy, S.J. , H.E. Hurlburt and J.J. O'Brien. The connectivity of eddy variability in the Caribbean Sea, the Gulf of Mexico, and the Atlantic Ocean. *J. Geophys. Res.*, **104** (C1), 1431-1453, 1999.

Özgökmen, T., E.P. Chassignet, and A. Paiva. Impact of wind forcing, bottom topography, and inertia on mid-latitude jet separation in a quasi-geostrophic model. *J. Phys. Oceanogr.*, **27**, 2460-2476, 1997.

Richardson, P.L., and D. Walsh. Mapping climatological seasonal variations of surface currents in the tropical Atlantic using ship drifts. *J. Geophys. Res.*, **91**, 10537-10550, 1986.

Richardson, P.L., and W.J. Schmitz. Deep cross-equatorial flow in the Atlantic measured with SOFAR floats, *J. Geophys. Res.*, **98**, 8371-8387, 1993.

Richardson, P.L., G.E. Hufford, R. Limeburner, and W.S. Brown. North Brazil Current retroflection eddies. *J. Geophys. Res.*, **99(C3)** 5081-5093, 1994.

Rintoul, S.. South Atlantic interbasin exchange. *J. Geophys. Res.*, **96**, 2675-2692, 1991.

Simmons, H.L. and D. Nof. The squeezing of eddies through gaps. *J. Phys. Oceanogr.*, **32**, 314-335, 2002.

Schott, F.A., J. Fischer and L. Stramma. Transports and pathways of the upper-layer circulation in the western tropical Atlantic, *J. Phys. Oceanogr.*, **28**, 1904-1928, 1998.

Schmitz, W.J.. On the World Ocean circulation: Volume 1. Some Global features North Atlantic Circulation. Woods Hole Oceanographic Institution Technical Report, WHOI-96-03, June, 1996.

Steve, D. M. and A. L. Brooks. Identification of Amazone River Water at Barbados, W. Indies, by Salinity and Silicate Measurements. *Mar. Biol*, **14**, 343-348, 1972.

Townsend, T., H.E. Hurlburt and P.J.Hogan. Modeled Sverdrup flow in the North Atlantic from 11 different wind stress climatologies. *Dyn. Atmosph. Oc.*, **32**, 373-417, 2000.

Wilson, D.W., W.E. Johns and S.L. Garzoli. Velocity structure of North Brazil Current rings, *Geophys. Res. Lett.*, **29**, doi=10.1029, 2002.